Luke Szymanski, Gurkan Gok, and Anthony Grbic

Controlling the amplitude and phase of antenna aperture fields.

# Beamforming With Multiple-Input, Multiple-Output Metastructures

he experimental realization of a multiple-input, multiple-output (MIMO) metastructure for antenna beamforming is reported. The metastructured beamformer is designed using a recently reported computational inverse design procedure that significantly reduces the required time and computational resources needed to design MIMO metastructures. This reduction in time and resources is achieved by circumventing full-wave simulations to evaluate device responses and using the adjoint variable method to evaluate gradients. To experimentally verify the MIMO metastructure's performance, the beamformer is patterned on a microwave substrate and interfaced with a 3D-printed aperture antenna to form a multibeam antenna. Measurement results for the multibeam antenna's performance are provided.

# INTRODUCTION

Metastructures are often designed to perform a single function, such as a polarization transformation [1], [2], refraction [3], [4],

Digital Object Identifier 10.1109/MAP.2022.3169391 Date of current version: 7 June 2022 or focusing [5]–[7]. However, there are many applications where it is desirable for a metastructure to be able to perform multiple functions, such as in imaging [8], antenna beamforming [9]–[11], or analog computing [12], [13]. One way that metastructures capable of performing multiple functions have been realized is through reconfigurability [14]–[16]. Reconfigurable metastructures utilize arrays of tunable unit cells that can be tailored to produce different responses. Using tunable unit cells is versatile but also has its drawbacks. They tend to have increased losses, possess finite switching times, and require bias circuitry and control logic. Therefore, for applications that require a finite set of predetermined functions, MIMO metastructures are an attractive alternative. MIMO metastructures do not require tunability nor control/bias circuitry, and they can be realized using low-loss unit cells.

However, efficient methods for designing MIMO metastructures are still needed. One route that is particularly promising for realizing high-performance MIMO metastructures is computational inverse design [11]–[13], [17]–[24].

Early work in computational inverse design focused on designing metastructures with a single functionality. But recently, it has also been used to design MIMO metastructures [11]–[13], [17]–[19]. Here, the focus is on using these methods to design a particular type of MIMO metastructure: a metastructured antenna beamformer. The inverse design procedure provided in [18] is used since it is well suited for the design of guided-wave devices that are electrically large, contain many subwavelength features, and possess a large number of design variables. It performs well on these types of problems because it circumvents full-wave simulations during the optimization process through the use of a circuit network solver and utilizes the adjoint variable method to efficiently calculate gradients.

To understand the potential benefits of using MIMO metastructures over more conventional methods for beamforming, such as Rotman lenses, planar Luneburg lenses, or Butler matrices, consider the following comparisons. Note that the following comparisons assume that the beamformers are implemented on microwave substrates, with  $\epsilon_r < 3$ , and are used to feed an antenna that is  $8 \lambda_0$  wide to allow for a quantitative comparison. Rotman lenses provide broadband performance, but they have curved interfaces and are relatively large in both their transverse and longitudinal dimensions  $(4-8 \lambda_0)$ . Additionally, they provide a maximum of three perfectly phased aperture fields and have no control over the aperture field's amplitude [25]. Planar Luneburg lenses are also broadband and produce identical aperture fields for all scan angles, but again, there is no control over the amplitude pattern [26]. They also possess curved interfaces and are quite large with a diameter of at least 8  $\lambda_0$ .

An alternative to quasi-optical beamformers are Butler matrices, which can theoretically produce an arbitrary number of perfectly phased aperture fields [27]. However, Butler matrices are typically narrowband, lossy, and have limited control over the amplitude of the aperture fields. They are also relatively large with a depth greater than  $4 \lambda_0$ . The advantage of using MIMO metastructures is that they can provide amplitude and phase control for all output fields, have planar interfaces that may be easier to integrate into various platforms, reduce the

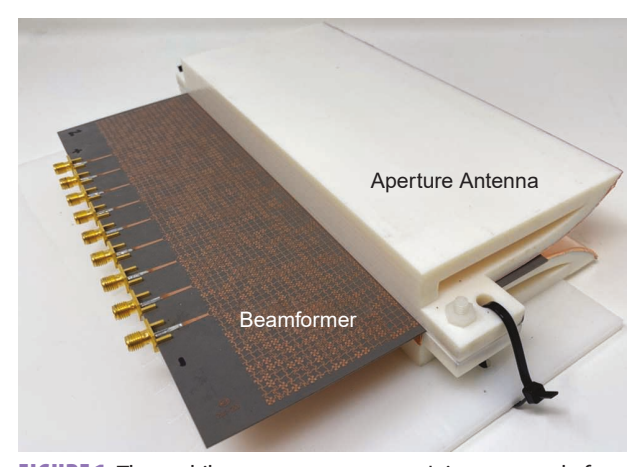


**FIGURE 1.** The multibeam antenna system. It is composed of a printed-circuit beamformer and a 3D-printed aperture antenna.

overall size of the beamforming region, and have the potential to operate over wide bandwidths, as demonstrated in [11].

This work reports the experimental realization of a metastructured beamformer that has been integrated with a 3D-printed aperture antenna. The metastructured beamformer is designed using the computational inverse design procedure proposed in [18], which is briefly reviewed and then applied. Measurements of the antenna's radiation patterns, return loss, and isolation demonstrate that the proposed design method can be used to design practical devices.

## MIMO METASTRUCTURE DESIGN PROCEDURE

The antenna beamformer for the multibeam antenna system, shown in Figure 1, is designed using the computational inverse design procedure for MIMO metastructures provided in [18]. The main advantage of this design procedure over others, such as the one provided in [11], is that it directly optimizes the patterned geometry of the metastructure in a computationally efficient manner. This enables the rapid synthesis of electrically large devices without the need for full-wave optimization. Full-wave simulations are avoided during runtime by using a 2D circuit network solver and the adjoint variable method to evaluate gradients in the quasi-newton optimization procedure. This section contains a brief review of the design procedure; for the details, refer to [18].

### THE 2D CIRCUIT NETWORK SOLVER

Designing metastructures through computational inverse design requires the selection of a forward problem solver to evaluate device responses. To make the design of electrically large MIMO devices tractable, the forward problem solver should be able to evaluate device responses quickly and accurately. Full-wave solvers provide a high level of accuracy, but when devices are electrically large and contain many subwavelength features, which is common in metastructured devices, they consume significant computational resources and are prohibitively slow. Therefore, it is desirable to avoid the use of full-wave solutions during the optimization process, if possible.

For 2D metastructures supporting guided waves, this can be achieved by representing the device as a 2D circuit network composed of four-port admittance matrices (representing the unit cells) tiled in the xz-plane, as shown in Figure 2. By representing the problem in this way, macroscale or device level effects are accounted for by modeling the interactions between neighboring unit cells using circuit theory, and microscale or unit cell level effects are accounted for by using a reduced-order model of the unit cell's admittance matrix. The accuracy of these models can be maintained by using full-wave simulations to generate the reduced-order models. Accuracy is then limited only by the number of accessible modes that are accounted for by the admittance matrices [28]. If all of the accessible modes at the ports of the unit cell are included in the model, then it is a perfect representation of the unit cell's response. However, if the unit cell supports a single propagating mode, and all other modes are well below their cutoff frequency, then a single guided mode can be used to obtain satisfactory results, as is shown here.

## THE OPTIMIZATION PROCEDURE

Here, the design of MIMO metastructures is posed as an optimization problem over the unit cell's characteristics (design variables). The design procedure starts with a set of excitations (inputs) and their desired responses (outputs). Since a circuit network solver is used, the excitations are specified as voltage distributions along the input plane, and the desired responses are voltage distributions along the boundaries of the network (see Figure 2). The inputs are referred to as  $\{\mathbf{v}_{\text{in}}^k\}$  and the outputs as  $\{\mathbf{v}_{\text{out}}^k\}$ , where  $k \in \{1,2,3,...,K\}$  and K is the total number of input–output pairs. An input–output pair refers to an input voltage distribution and its associated output voltage distribution. The total cost function is formed by defining a partial cost function  $g_k(\mathbf{p})$  that captures the error in the output for each input–output pair

$$g_k(\mathbf{p}) = \frac{1}{2} (\mathbf{v}^k(\mathbf{p}) - \mathbf{v}_{\text{out}}^k)^H \bar{\bar{G}} (\mathbf{v}^k(\mathbf{p}) - \mathbf{v}_{\text{out}}^k), \tag{1}$$

where  $\mathbf{p}$  is a vector containing all of the design variables in the network, the vector  $\mathbf{v}^k(\mathbf{p})$  contains the voltages in the network (subject to the design variables) when it is excited by  $\mathbf{v}_{\text{in}}^k$ , and the superscript H indicates the conjugate transpose. The matrix  $\bar{G}$  acts as a mask and is used to select and scale the elements of  $\mathbf{v}^k(\mathbf{p}) - \mathbf{v}_{\text{out}}^k$ . The total cost function is then formed by summing over all of the input–output pairs as follows

$$g(\mathbf{p}) = \sum_{k=1}^{K} g_k(\mathbf{p}). \tag{2}$$

Using (2), the following optimization problem can be defined to design MIMO devices

where  $\mathbf{p}_{lb}$  and  $\mathbf{P}_{ub}$  are vectors containing the lower and upper bounds of the design variables, respectively. To solve (3), a quasi-Newton optimization routine is employed that uses the adjoint variable method to calculate the gradient. Further details regarding the optimization procedure are provided in [18].

### **MULTIBEAM ANTENNA DESIGN**

In this section, a multibeam antenna system that produces nine switched beams and operates at 10 GHz is designed. The multibeam antenna system consists of a printed-circuit beamformer that is integrated with a 3D-printed aperture antenna. The printed-circuit beamformer is designed by using a transmission-line unit cell in the design procedure outlined in the "MIMO Metastructure Design Procedure" section. A transmission-line unit cell is selected because it provides a wideband response and is planar, compact, low cost, and amenable to printed-circuit

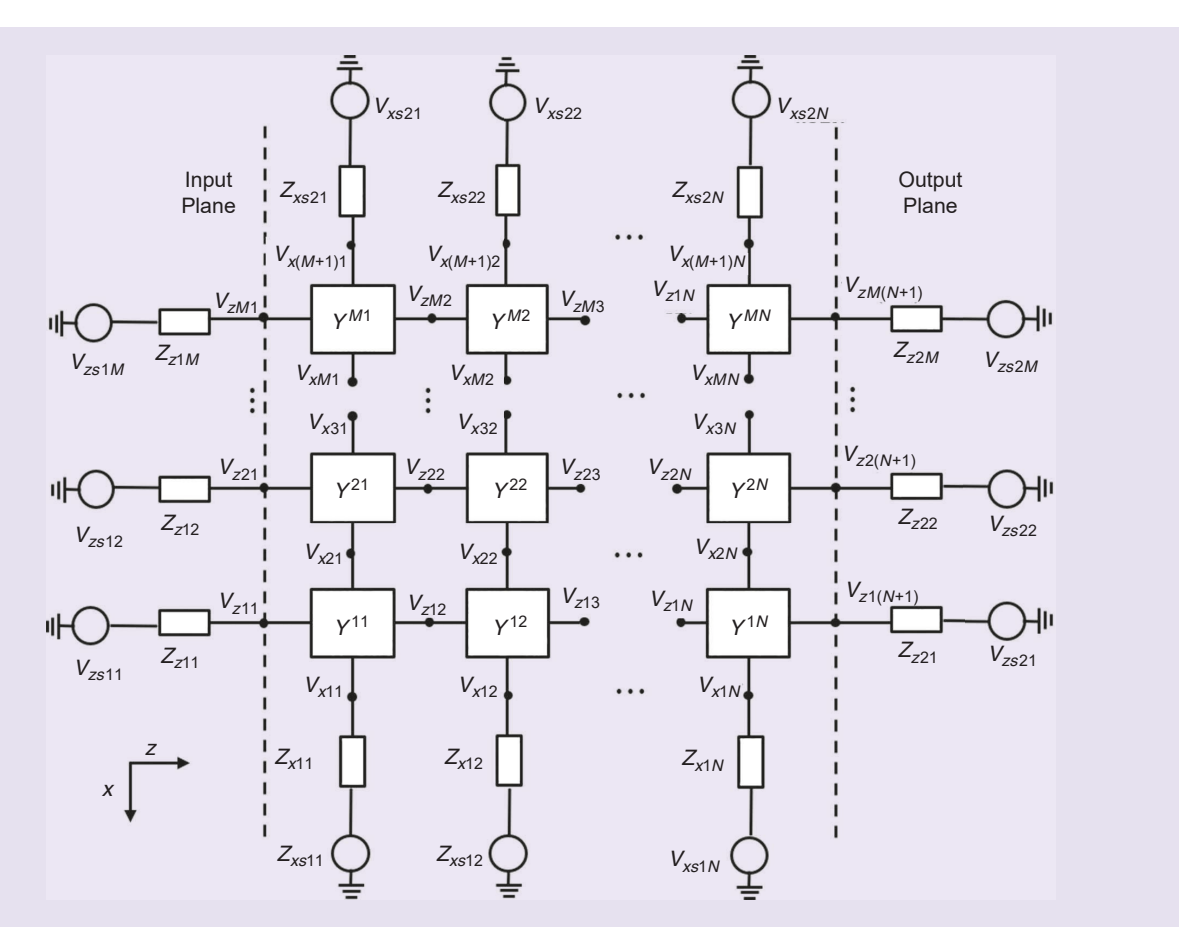


**FIGURE 2.** A metastructure consisting of an M-by-N grid of four-port admittance matrices. The admittance matrices represent the metastructure's unit cells. Lumped impedances and voltages along the boundaries are used to excite the metastructure and produce the desired boundary conditions.

processes. The aperture antenna is then designed to be integrated with the beamformer and provides broadband impedance matching for all nine excitations.

## **BEAMFORMER DESIGN**

The printed-circuit beamformer is designed to feed an aperture antenna, designed in the "Antenna Design" section (see Figure 1), and is patterned on a Roger's RT/Duroid RO5880 substrate,  $\epsilon_r = 2.2$  and  $\tan \delta = 0.0009$ , with a substrate thickness of h = 0.787 mm and a copper thickness of  $35~\mu \mathrm{m}$ . The width of the beamformer is chosen to match the width of the antenna's input aperture, i.e.,  $W = 24~\mathrm{cm}~(8\lambda_0)$ , and the depth of the beamformer is chosen to be  $D = 6~\mathrm{cm}~(2\lambda_0)$ . This depth is chosen to minimize the size of the beamforming network while allowing for the power distribution at the aperture to be shaped without utilizing cavity effects from the edges of the beamformer.

Since the design procedure outlined in the "MIMO Metastructure Design Procedure" section is used, the following steps are required to properly define the problem.

- 1) The beamforming region must be discretized.
- 2) A unit cell topology must be selected.
- 3) A model of the unit cell needs to be developed.
- 4) The design goals need to be stated in terms of an output voltage profile for each input.

First, the beamforming region is discretized into square unit cells with a side length of d=3 mm ( $\lambda_0/10$ ). This discretization corresponds to a grid of unit cells modeled with admittance matrices (see Figure 2). The grid has 80 unit cells in the x-direction (M=80) and 20 unit cells in the z-direction (N=20).

Next, the microstrip unit cell topology, shown in Figure 3, is selected. The unit cell has 6 degrees of freedom: two

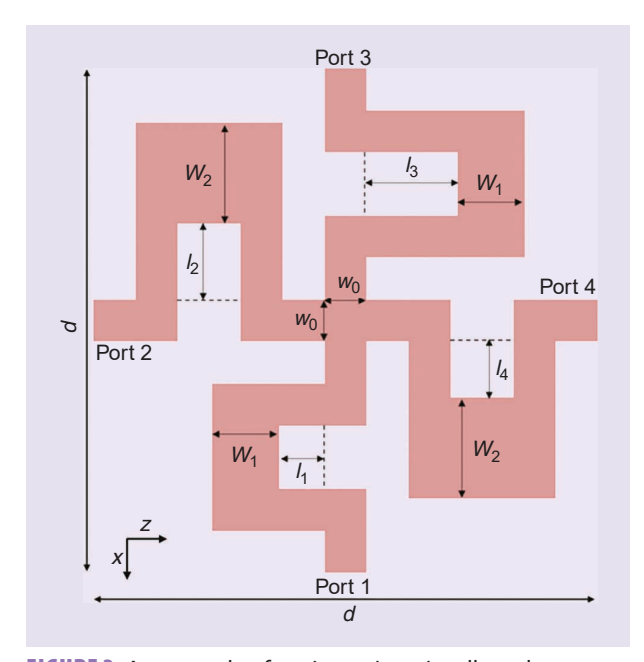


**FIGURE 3.** An example of a microstrip unit cell used to design the metastructured beamformer. The unit cell is parameterized using six design variables:  $W_1$ ,  $W_2$ ,  $I_1$ ,  $I_2$ ,  $I_3$ , and  $I_4$ . The microstrip lines all have a width of  $w_0 = 0.25$  mm except for the lines with widths  $W_1$  or  $W_2$ .

transmission-line widths and four transmission-line lengths. The variable width lines are allowed to vary from 0.2 mm to 0.8 mm and have a length of 0.875 mm. The variable length lines have a width of  $w_0 = 0.25 \,\mathrm{mm}$ , and their lengths are allowed to vary from 0 to  $l_i^{\text{max}}$ . The variable  $l_i^{\text{max}} = d/2 - w_0/2 - W_j$ , and  $W_i$  corresponds to the variable width line connected to  $l_i$  for  $i \in \{1,2,3,4\}$ . This is the same unit cell used in [18]. It was chosen to balance the unit cell's complexity with the number of degrees of freedom as well as the variables' ability to control the unit cell's admittance parameters. To create a differentiable model of the unit cell, a database of 15,625 unit cells was simulated in the commercial method of the moments solver Keysight Momentum to determine their admittance parameters at 10 GHz. For these simulations, the substrate and conductors were assumed to be lossless, and the conductors had no thickness or surface roughness. The database of simulated admittance parameters was then spline interpolated to generate a model of the unit cell for use in the design procedure.

To state the design goals in terms of output voltage profiles along the boundaries of the grid, the desired characteristics of the beamformer need to be specified. The beamformer is designed to operate at 10 GHz and produce nine beams that are excited by nine different 50- $\Omega$  input ports. The input ports are impedance matched and isolated from each other to allow for the beams to be simultaneously excited. During the design process, the beamformer is assumed to be lossless, which, combined with the condition of isolated input ports, requires the antenna's radiation patterns to be mutually orthogonal [29]. For this reason, the radiation patterns are chosen to be sinc functions with beam-pointing directions corresponding to the following tangential wave numbers

$$k_n = \frac{2\pi n}{Md}, \ n \in \{0, \pm 1, \pm 2, \pm 3, \pm 4\}.$$
 (4)

In (4), d is the physical spacing between the beamformer output ports, and M is the number of output ports. For M and d in this design, the wavenumbers given by (4) correspond to the following beam-pointing directions:  $\theta_B = 0^{\circ}, \pm 7.18^{\circ}, \pm 14.48^{\circ}, \pm 22.02^{\circ}, \pm 30^{\circ}$ . The aperture fields corresponding to these radiation patterns are uniform amplitude with linear phase gradients given by (4). These aperture fields are the target output voltage profiles along the output plane of the beamformer, shown in Figure 2. To ensure that the input ports are isolated and reduce reflections from the edges of the beamformer, the desired output voltages at the remaining nodes along the periphery of the beamformer, besides those corresponding to the active input port, are set to zero. The voltages at the nodes corresponding to the active input port are used to ensure impedance matching. Since the nodes are terminated by a matched impedance and excited by a voltage  $V_n$ , the desired output voltage is  $V_n/2$  to ensure that the port is impedance matched.

The two remaining considerations before designing the beamformer are determining how to excite the beamforming region and how to terminate the grid of admittance matrices. The beamforming region will be excited along the input plane by exciting pairs of nodes starting from the center line of the beamformer. Each of the pairs is separated by 1.2 cm (see Figure 4). Exciting pairs of nodes serves two purposes: 1) it maintains symmetry in the beamformer and 2) it makes impedance matching the microstrip lines with width  $w_0$  ( $Z_0 \approx 147~\Omega$ ) at the unit cell's ports to 50  $\Omega$  easier. It makes impedance matching easier because it reduces the input impedance of the combined lines to 73.5  $\Omega$ .

Practically, the ports are combined by terminating the grid in microstrip lines with  $Z_0=147~\Omega$  and then using a T-junction to combine them in parallel, as shown in Figure 4. Each pair of lines is then impedance matched to  $50~\Omega$  using a tapered-impedance microstrip line with a length of 2 cm. Therefore, in the circuit network solver, the input ports are terminated by  $147~\Omega$  lumped impedances.

The output plane of the admittance matrix grid should be impedance matched to the parallel-plate waveguide that the beamformer is terminated in. Since each of the output ports excites a section of the parallel-plate waveguide that is d=3 mm wide, the output terminations correspond to the following transverse electric wave impedances for each of the beam-pointing directions  $\theta_B$ 

$$Z_{\text{out}} = \frac{\eta_0}{\sqrt{\epsilon_r} \cos \theta_B} \frac{h}{d} = \frac{66.7 \,\Omega}{\cos \theta_B},\tag{5}$$

where  $\eta_0$  is the free-space wave impedance and  $\epsilon_r$  is the dielectric constant of the substrate. The terminations for the remaining ports along the input plane and the sides of the beamformer are assumed to be open circuits. Combined with the target of zero voltage at these nodes, this allows the cost function to select designs with lower reflections from the edges of the beamformer.

With the design goals and terminations defined, the beamforming region can now be designed. However, before designing the beamformer, symmetries can be exploited to reduce the number of variables and improve convergence. The symmetry of the aperture fields and excitations across the center line of the metastructure allows for the number of design variables to be reduced from 9,600 to 4,800. This is achieved by mirroring the admittance matrices across the center line. After enforcing symmetry in the circuit network solver, the beamformer is designed by providing the optimization routine with the unit cell model, the excitations (input voltage profiles), and the desired outputs (output voltage profiles), along with a seed of uniform lengths and widths for the design variables.

The algorithm was run on a personal computer with an i7-9700 CPU at 3 GHz with eight cores and 64 GB of random-access memory (RAM) and was set to terminate after 400 iterations. After approximately 5.5 h of execution, the design shown in Figure 4 was produced. The design has a minimum return loss of 26.4 dB for ports  $n=\pm 4$ , a minimum isolation of 21 dB between ports  $n=\pm 2$  and  $n=\pm 3$ , and produces the radiation patterns shown in Figure 5. These radiation patterns are calculated analytically assuming that the aperture field is piecewise uniform in amplitude and phase.

To verify the performance of the beamformer, a full-wave simulation was performed in the commercial electromagnetics solver Keysight Momentum. As in the unit cell simulations, the substrate and conductors were assumed to be lossless, and the conductors had no thickness or surface roughness. It took approximately 94 h to complete on a high-performance computing cluster with access to 15 cores and 600 GB of RAM. The full-wave results show good agreement, showing only a slight degradation in performance. The minimum return loss is 19.1 dB for ports  $n = \pm 1$ , the minimum isolation is 18.3 dB between ports n = -2 and n = 2, and the voltages at the output of the beamformer produce the radiation patterns shown in Figure 5. Again, these radiation patterns are calculated analytically assuming that the aperture field is piecewise uniform in amplitude and phase. Overall, the performance is in good agreement with that predicted by the circuit network solver.

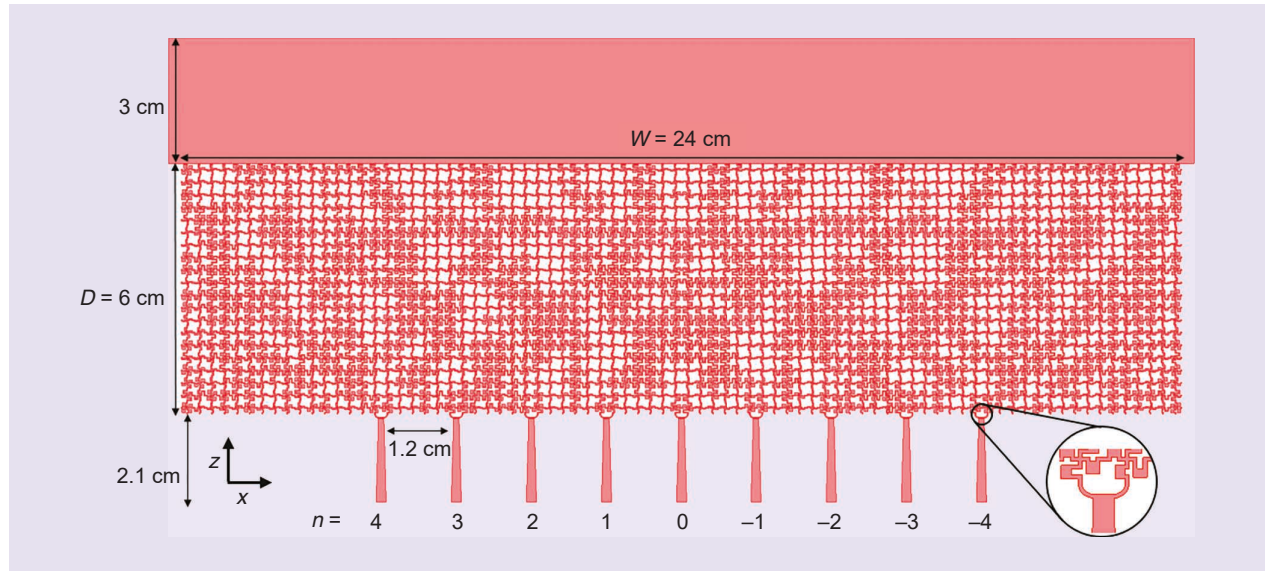


**FIGURE 4.** The layout of the metastructured beamformer. The beamformer is fed by nine input ports and is terminated in a parallel-plate waveguide. The beamformer's input ports are labeled  $n=0,\pm1,\pm2,\pm3,\pm4$ , which produce aperture fields with phase gradients that correspond to transverse wavenumbers given by (4).

# **ANTENNA DESIGN**

The 3D-printed flared aperture antenna has a center frequency of 10 GHz and is designed to operate over a broad bandwidth. It is fed by a parallel-plate waveguide and transitions waves propagating in the transverse electromagnetic mode to radiated waves in free space. The antenna interfaces with the printed-circuit beamformer designed in the "2D Circuit Network Solver" section. Therefore, the parallel-plate waveguide feeding the antenna is a copper-clad substrate. In this particular design, it is a 24-cm-wide piece of a Roger's RT/Duroid RO5880 substrate,  $\varepsilon_r=2.2$  and  $\tan\delta=0.0009$ , with a substrate thickness of h=0.787 mm and a copper thickness of 35  $\mu$ m. The antenna's input aperture has the same dimensions as the parallel-plate waveguide feed, i.e.,  $W_{\rm in}=24$  cm and  $h_{\rm in}=0.787$  mm, and the aperture is tapered in the E-plane to the final dimensions  $W_{\rm ap}=24$  cm and  $h_{\rm ap}=5$  cm (see Figure 6).

The antenna is impedance matched to the parallel-plate waveguide feed using an E-plane taper and a piece of substrate that is extended into the antenna's aperture, shown in Figure 6. To allow for broadband impedance matching, the height of the aperture is tapered exponentially from  $h_{\rm in}$  to  $h_{\rm ap}$  over a length of  $L_{\rm taper}=7.5$  cm. To avoid an impedance mismatch at the junction between the dielectric-filled parallel-plate waveguide feed and the air-filled parallel-plate waveguide at the antenna's input, a piece of substrate with length  $L_{\rm sub}=3$  cm is extended into the antenna. The substrate allows for the dielectric filling fraction within the antenna to be slowly tapered. This tapers the wave impedance and avoids large reflections at the interface. Alternatively, the height of the air-filled waveguide could have been reduced to  $h_{\rm in}=0.53$  mm to match the impedance of the

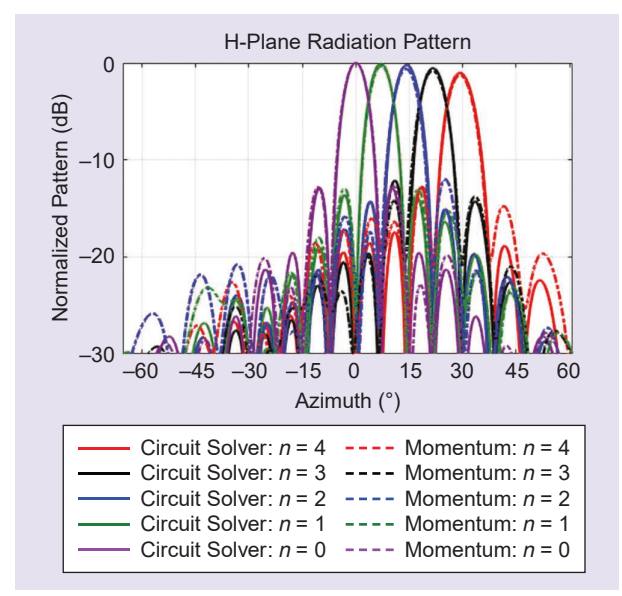


**FIGURE 5.** The analytically calculated copolarized H-plane radiation patterns produced by an aperture antenna fed by the metastructured beamformer. The solid lines are calculated using the simulated voltages from the circuit network solver. The dot-dashed lines are calculated using the simulated voltages from the full-wave (Keysight Momentum) simulation. For clarity, only the positive scan angles are shown. The negative scan angles are identical due to symmetry.

two waveguides. However, for ease of fabrication, the former method for impedance matching was chosen.

The two lengths  $L_{\rm taper} = 7.5$  cm and  $L_{\rm sub} = 3$  cm were chosen by performing parametric sweeps in Ansys high-frequency structure simulator (HFSS) simulations. First, a 3-mm-wide section of the antenna was simulated in a periodic environment, and  $L_{\rm sub} = 3$  cm was swept to find the minimum length such that  $|S_{11}|$  did not decrease with an increase in  $L_{\rm sub}$ . Next, the same periodic simulation was run, and  $L_{\rm taper}$  was swept until  $|S_{11}|$  was less than -10 dB between 8 and 12 GHz for all scan angles.

The full antenna structure, shown in Figure 6, was then simulated in Ansys HFSS to verify its performance. The antenna was then excited using the simulated output voltages of the beamformer for each scan angle, and the H-plane radiations patterns are shown in Figure 7. A maximum directivity of  $D_0 = 20.6~\mathrm{dB}$  was observed for the broadside radiation pattern, indicating that the antenna has a maximum aperture efficiency of 68%.

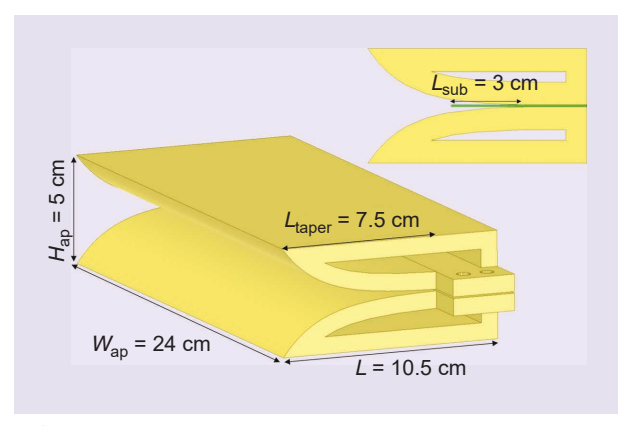


**FIGURE 6.** A rendering of the 3D-printed aperture antenna and its dimensions. A depiction of the piece of substrate, with length  $L_{\text{sub}}$ , that is extended into the antenna's aperture for impedance matching is shown in the top right.

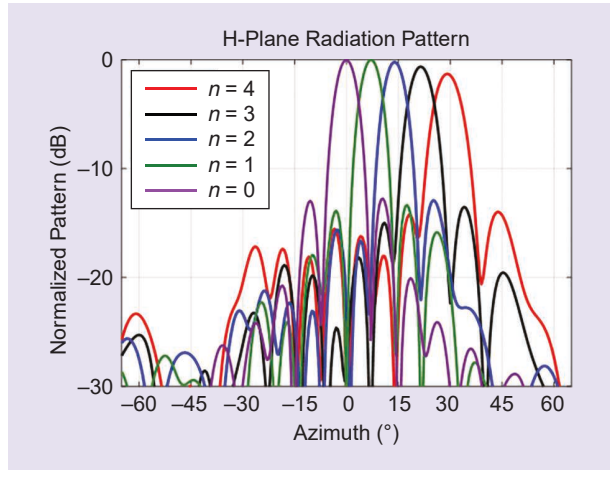


FIGURE 7. The full-wave simulation results of the copolarized H-plane radiation patterns from the 3D-printed aperture antenna. The plots are produced by exciting the simulated antenna (Ansys HFSS) with the output voltages from the full-wave simulation (Keysight Momentum) of the metastructured beamformer. For clarity, only the positive scan angles are shown. The negative scan angles are identical due to symmetry.

It should be noted that the reduction in aperture efficiency is because the electric field in E-plane is not uniform at the end of the tapered aperture. The antenna was then manufactured with a Stratasys J750 PolyJet 3D printer using Verowhite material, and the tapered aperture was metallized using copper tape. A picture of the manufactured antenna is shown in Figure 8.

### **MEASUREMENT RESULTS**

In this section, measurement results for the multibeam antenna are reported. The multibeam antenna was assembled by inserting the parallel-plate waveguide at the end of the patterned substrate into the aperture at the antenna's input. The antenna was then fastened to the beamformer with nylon screws, as shown in Figure 9. In the following sections, measurement results for the antenna's return loss, input isolation, and radiation patterns are provided.

## **RETURN LOSS AND ISOLATION**

In this section, the following nomenclature for the ports is adopted. The ports are numbered from left to right such that port 1 corresponds to n = 4, and port 9 corresponds to n = -4.

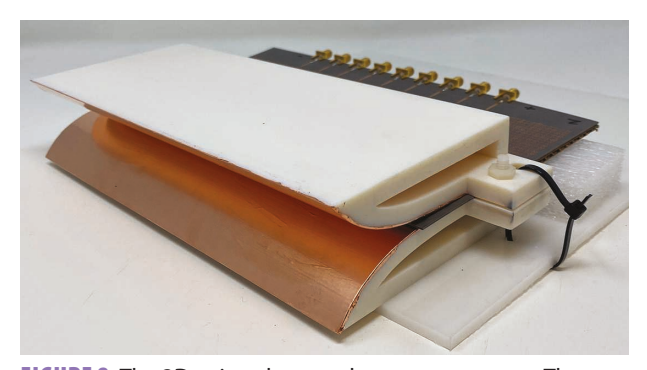


**FIGURE 8.** The 3D-printed tapered aperture antenna. The aperture of the 3D-printed part has been coated with copper tape to make it conductive.

The performance of the input ports was measured using a Keysight E8361A PNA Network Analyzer. To characterize the return loss for each port  $S_{ii}$ ,  $i \in \{1,2,...,9\}$ , was measured from 8 to 12 GHz while terminating all other ports with broadband  $50 \cdot \Omega$  loads. The results for all of the ports are shown in Figure 10. A return loss greater than 10 dB was measured over a bandwidth (range of frequencies) of 1.5 GHz.

Next, the port-to-port isolation was characterized from 8 to 12 GHz by connecting all possible pairs of ports one at a time and measuring  $S_{ij}$ ,  $i,j \in \{1,2,...,9\}$ , while the remaining ports were terminated in 50- $\Omega$  loads. By inspecting  $S_{ii}$  and  $S_{ij}$  for all of the ports, a frequency shift is observed in the beamformer's performance. The frequency that maximizes the return loss and isolation for the port with the minimum return loss and isolation is 10.2 GHz. This indicates that the beamformer's operating

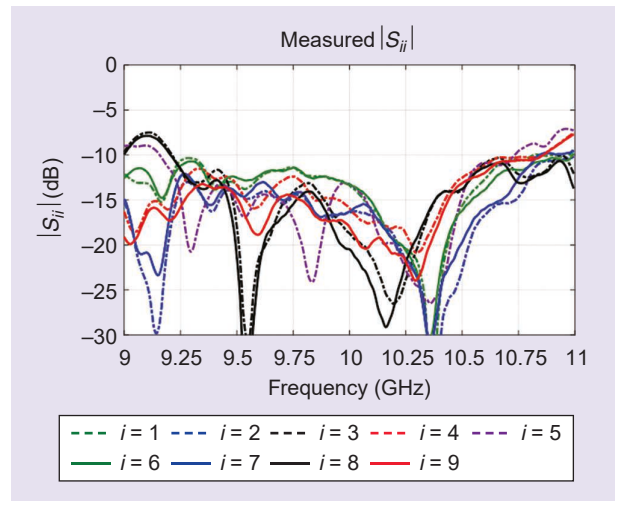


**FIGURE 10.** Plots of the measured reflection coefficient magnitudes ( $|S_{ii}|$ ) for the multibeam antenna's input ports from 9 to 11 GHz.

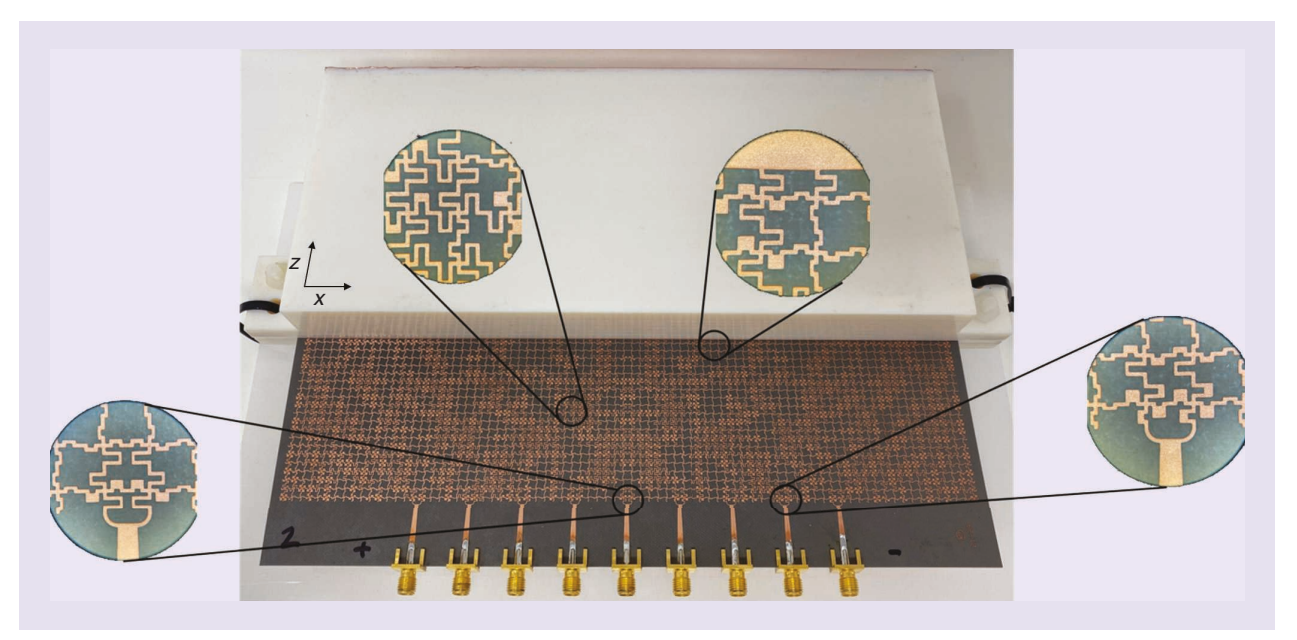


FIGURE 9. The patterned metastructured beamformer connected to the 3D-printed aperture antenna.

frequency has shifted to 10.2 GHz. The values for the return loss and isolation at this frequency are reported in Table 1 and Table 2, respectively.

| TABLE 1. INPUT RETURN LOSS. |                    |                     |  |  |
|-----------------------------|--------------------|---------------------|--|--|
| Port                        | Simulated (10 GHz) | Measured (10.2 GHz) |  |  |
| 1                           | 25.9 dB            | 18.1 dB             |  |  |
| 2                           | 27 dB              | 26.6 dB             |  |  |
| 3                           | 20.7 dB            | 18.9 dB             |  |  |
| 4                           | 19.1 dB            | 19.4 dB             |  |  |
| 5                           | 25.5 dB            | 19.8 dB             |  |  |
| 6                           | 19.1 dB            | 19.3 dB             |  |  |
| 7                           | 20.7 dB            | 19.5 dB             |  |  |
| 8                           | 27 dB              | 27.1 dB             |  |  |
| 9                           | 25.9 dB            | 20.9 dB             |  |  |
|                             |                    |                     |  |  |

| TABLE 2. INPUT ISOLATION AT 10.2 GHz. (I AND J REFER TO THE PORT INDICES. ALL VALUES ARE IN dB.) |      |      |      |      |      |      |      |      |
|--|------|------|------|------|------|------|------|------|
| i∖j  | 2    | 3    | 4    | 5    | 6    | 7    | 8    | 9    |
| 1  | 26.5 | 28.5 | 28.7 | 38.1 | 33.9 | 33.8 | 31.2 | 25.2 |
| 2  | _    | 24.3 | 27.5 | 28.3 | 32.6 | 44.9 | 25.5 | 33.2 |
| 3  | _    | _    | 22.9 | 30.8 | 33.7 | 21.7 | 39.7 | 36.3 |
| 4  | _    | _    | _    | 27.3 | 19.2 | 38.4 | 31.3 | 33.2 |
| 5  | _    | _    | _    | _    | 28.1 | 35.1 | 29   | 45.9 |
| 6  | _    | _    | _    | _    | _    | 23.3 | 26.9 | 30   |
| 7  | _    | _    | _    | _    | _    | _    | 23.8 | 28.5 |
| 8  | _    | _    | _    | _    | _    | _    | _    | 31.2 |
|  |      |      |      |      |      |      |      |      |

# **RADIATION PATTERNS**

The antenna's far-field radiation patterns were measured in an anechoic chamber using a HP-83592A signal generator and an HP-8592L spectrum analyzer. Measured results for the radiation patterns are shown for  $f=10.2~\rm GHz$  rather than  $f=10~\rm GHz$ . It should be noted that the beamformer was not optimized for bandwidth and is narrowband. The 10-dB sidelobe level and 3-dB gain bandwidths are 4%. As noted in the "Return Loss and Isolation" section, the measurement frequency was determined by selecting the frequency that maximized the minimum return loss and isolation of all of the input ports. The copolarized and cross-polarized H-plane radiation patterns were measured for all nine beams. The results for the copolarized measurement are shown in Figure 11(a). Good agreement is shown with the simulated patterns in terms of the main beam and first sidelobes.

The largest discrepancy is in the outer sidelobes for the beams at  $\theta_B = \pm 30^\circ$ , which are approximately 3 dB greater than the simulated value. The elevated sidelobes are most likely due to amplitude errors resulting from manufacturing errors in the beamformer and warping in the antenna that degrades the contact between the antenna and the parallel-plate waveguide on the printed circuit board. The cross-polarized measurements are shown in Figure 11(b), verifying that the cross-polarized radiation is low. Additionally, the copolarized and cross-polarized E-plane radiation patterns are measured for the n = 0 (broadside) beam. The radiation patterns for these measurements are shown in Figure 12(a) and (b). The copolarized E-plane radiation pattern shows good agreement with the simulated result between  $-25^{\circ}$  and  $15^{\circ}$ . The discrepancies between the measured and simulated radiation patterns outside of this range of angles are most likely a result of warping in the surface of the manufactured antenna's aperture.

Using the 3-dB beamwidths of the E- and H-plane radiation patterns for the broadside beam, the maximum directivity

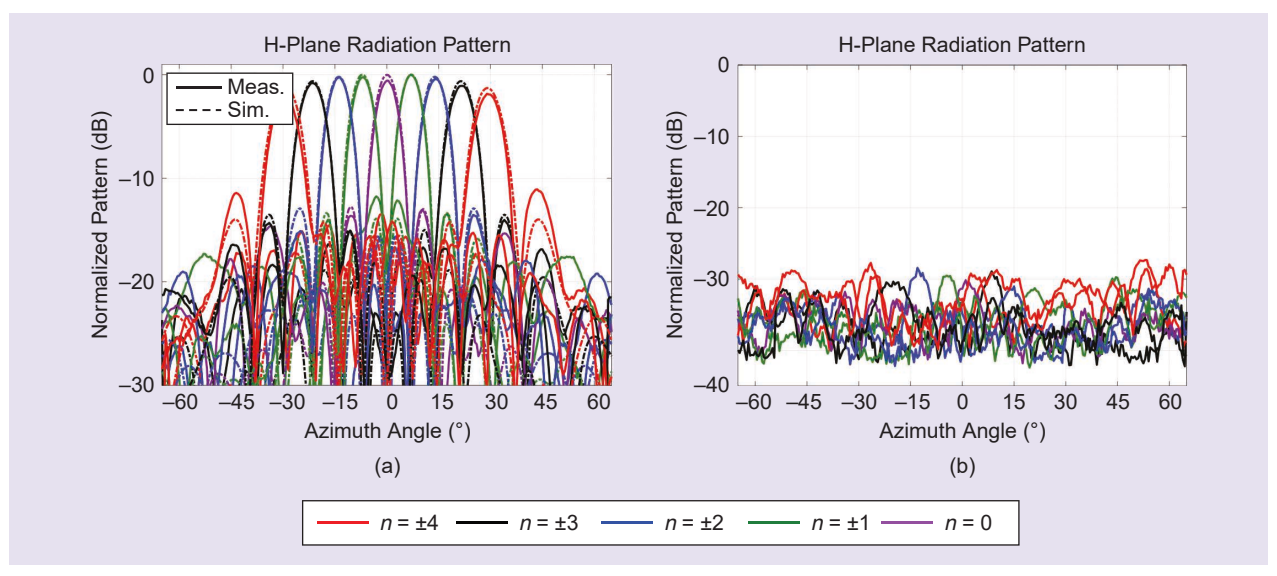
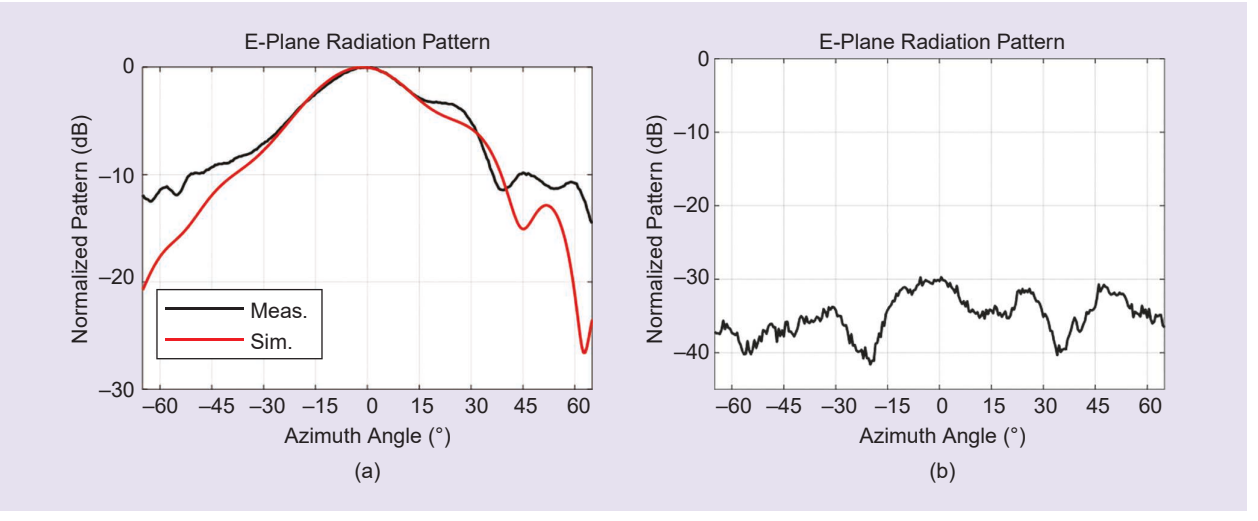


FIGURE 11. (a) A comparison of the measured and simulated copolarized H-plane radiation pattern for all nine inputs. The measured radiation patterns are the solid lines and the simulated radiation patterns are the dot-dashed lines. (b) The measured cross-polarized H-plane radiation pattern for all nine inputs, normalized by the maximum of the copolarized radiation pattern for the same input. Meas.: measured; Sim.: simulation.



**FIGURE 12.** (a) A comparison of the measured and simulated copolarized E-plane radiation pattern for the broadside beam (n = 0). (b) The measured cross-polarized E-plane radiation pattern for the broadside beam, normalized by the maximum of the copolarized radiation pattern for the same input.

|        | LE 3. APPROXIMAT<br>R THE BROADSIDI<br>Simulated |         |
|--------|--|---------|
| [30]   | 22 dB  | 22 dB   |
| [31]   | 18.4 dB  | 18.2 dB |
| Actual | 20.6 dB  | _       |

|    | TABLE 4. MEASURED GAIN. |  |  |
|----|-------------------------|--|--|
| n  | Gain                    |  |  |
| -4 | 16.1 dB                 |  |  |
| -3 | 16.8 dB                 |  |  |
| -2 | 17.5 dB                 |  |  |
| -1 | 17.9 dB                 |  |  |
| 0  | 17.9 dB                 |  |  |
| 1  | 17.6 dB                 |  |  |
| 2  | 17.6 dB                 |  |  |
| 3  | 17.1 dB                 |  |  |
| 4  | 15.8 dB                 |  |  |

of the measured antenna is approximated using formulas from [30] and [31]. These values are compared to approximations of the simulated antenna's directivity using the simulated 3-dB beamwidths in the E- and H-planes. As seen in Table 3, the measured values are in close agreement with those from the simulation. This indicates that the actual directivity of the manufactured antenna should be close to the simulated directivity of  $D_0 = 20.6$  dB. To characterize the efficiency of the antenna, the gain for each scan angle was measured using a standard gain horn and the gain-transfer method [32].

The measured gains for all nine beams are shown in Table 4. Comparing these values to the simulated directivity indicates

that there is approximately 2.7 dB of loss for the broadside beam. The loss should be close to 2.7 dB for all of the excitations due to the good agreement between the measured and simulated H-plane patterns seen in Figure 11(a). This is similar to the simulated loss provided in [26], which was between 2.4 and 2.9 dB between 9 and 12 GHz and is better than a Rotman lens, which is typically around 3 dB [33], or the metamaterial-based beamformer in [17], which was greater than 4.6 dB in simulation.

# CONCLUSION

A multibeam antenna system using a metastructured beamformer integrated with a 3D-printed aperture antenna was reported. A previously reported computational inverse design procedure for MIMO metastructures was used to design the beamformer. The design procedure uses a fast, forward solver that leverages circuit theory to circumvent the use of full-wave simulations and uses the adjoint variable method to calculate gradients. This approach significantly reduces the computational cost of designing MIMO metastructures that are electrically large and aperiodic, like antenna beamformers.

To validate the design procedure, the metastructured beamformer was patterned on a microwave substrate and integrated with a 3D-printed aperture antenna. The measured performance of the antenna system was shown to be in good agreement with the simulated results, after accounting for a frequency shift in the manufactured beamformer. The work demonstrates that the design procedure is able to design devices that can be realized in practice.

The reported beamformer illustrates some of the advantages that MIMO metastructures provide over other beamforming methods. It demonstrates their ability to maintain planar interfaces, control the amplitude and phase of all aperture fields, and reduce the size of the beamformer. Future work will tackle the beamformer's narrow bandwidth and mitigate amplitude and phase errors present in the aperture fields. Potential methods

for improving the bandwidth are the inclusion of multiple frequencies in the cost function and introducing lossy terminations to mitigate reflections. The accuracy of the aperture fields could potentially be improved by using better models of the unit cells. This could be achieved by modeling the unit cells more accurately using multimodal admittance matrices to capture higher-order coupling between the unit cells.

## **ACKNOWLEDGMENTS**

This work was supported by the National Science Foundation under GOALI Grant 1807940. This research was supported in part through computational resources and services provided by Advanced Research Computing, a division of Information and Technology Services, at the University of Michigan, Ann Arbor. Anthony Grbic is the corresponding author.

# **AUTHOR INFORMATION**

Luke Szymanski (ljszym@umich.edu) is with the Department of Electrical Engineering and Computer Science, University of Michigan, Ann Arbor, Michigan, 48109, USA. His research interests include applied electromagnetics, metamaterials, computational inverse design, and radar imaging. He is a Student Member of IEEE.

*Gurkan Gok* (gurkan.gok@rtx.com) is the senior manager of the Electromagnetics and Network Team with the Raytheon Technologies Research Center, East Hartford, Connecticut, 06118, USA. His research interests include applied electromagnetics, metamaterials, microwave and photonic circuits, and sensors. He is a Member of IEEE.

Anthony Grbic (agrbic@umich.edu) is a professor with the Department of Electrical Engineering and Computer Science at the University of Michigan, Ann Arbor, Michigan, 48109, USA. His research interests include electromagnetic theory, engineered electromagnetic structures, antennas, and microwave circuits. He is a Fellow of IEEE.

# **REFERENCES**

- [1] D.-H. Kwon and D. H. Werner, "Polarization splitter and polarization rotator designs based on transformation optics," *Opt. Exp.*, vol. 16, no. 23, pp. 18,731–18,738, Nov. 2008, doi: 10.1364/OE.16.018731.
- [2] C. Pfeiffer and A. Grbic, "Bianisotropic metasurfaces for optimal polarization control: Analysis and synthesis," *Phys. Rev. Appl.*, vol. 2, no. 4, p. 044011, Oct. 2014, doi: 10.1103/PhysRevApplied.2.044011.
- [3] J. P. S. Wong, A. Epstein, and G. V. Eleftheriades, "Reflectionless wide-angle refracting metasurfaces," *IEEE Antennas Wireless Propag. Lett.*, vol. 15, pp. 1293–1296, Dec. 2015, doi: 10.1109/LAWP.2015.2505629.
- [4] C. Pfeiffer and A. Grbic, "Metamaterial Huygens' surfaces: Tailoring wave fronts with reflectionless sheets," *Phys. Rev. Lett.*, vol. 110, no. 19, p. 197,401, May 2013, doi: 10.1103/PhysRevLett.110.197401.
- [5] P. R. West et al., "All-dielectric subwavelength metasurface focusing lens," Opt. Exp., vol. 22, no. 21, pp. 26,212–26,221, Oct. 2014, doi: 10.1364/OE.22.026212.
- [6] M. Khorasaninejad, W. T. Chen, R. C. Devlin, J. Oh, A. Y. Zhu, and F. Capasso, "Metalenses at visible wavelengths: Diffraction-limited focusing and subwavelength resolution imaging," *Science*, vol. 352, no. 6290, pp. 1190–1194, 2016. [Online]. Available: https://science.sciencemag.org/content/352/6290/1190, doi: 10.1126/science.aaf6644.
- [7] Y. Zhou, I. I. Kravchenko, H. Wang, J. R. Nolen, G. Gu, and J. Valentine, "Multilayer noninteracting dielectric metasurfaces for multiwavelength metaoptics," Nano Lett., vol. 18, no. 12, pp. 7529–7537, 2018, doi: 10.1021/acs.nanolett.8b03017.
  [8] J. Hunt et al., "Metamaterial apertures for computational imaging," Science, vol. 339, no. 6117, pp. 310–313, 2013. [Online]. Available: https://science.sciencemag.org/content/339/6117/310, doi: 10.1126/science.1230054.

- [9] D. González-Ovejero, G. Minatti, G. Chattopadhyay, and S. Maci, "Multi-beam by metasurface antennas," *IEEE Trans. Antennas Propag.*, vol. 65, no. 6, pp. 2923–2930, Jun. 2017, doi: 10.1109/TAP.2017.2670622.
- [10] O. Quevedo-Teruel, "Roadmap on metasurfaces," J. Opt., vol. 21, no. 7, p. 073002, 2019, doi: 10.1088/2040-8986/ab161d.
- [11] B. B. Tierney, N. I. Limberopoulos, R. L. Ewing, and A. Grbic, "A planar, broadband, metamaterial-based, transmission-line beamformer," *IEEE Trans. Antennas Propag.*, vol. 66, no. 9, pp. 4844–4853, Sep. 2018, doi: 10.1109/TAP.2018.2845444. [12] A. S. Backer, "Computational inverse design for cascaded systems of metasurface optics," *Opt. Exp.*, vol. 27, no. 21, pp. 30,308–30,331, Oct. 2019, doi: 10.1364/OE.27.030308.
- [13] N. Mohammadi Estakhri, B. Edwards, and N. Engheta, "Inverse-designed metastructures that solve equations," *Science*, vol. 363, no. 6433, pp. 1333–1338, 2019. [Online]. Available: https://science.sciencemag.org/content/363/6433/1333, doi: 10.1126/science.aaw2498.
- [14] Z. Wu, Y. Ra'di, and A. Grbic, "Tunable metasurfaces: A polarization rotator design," *Phys. Rev. X*, vol. 9, no. 1, p. 011036, Feb. 2019, doi: 10.1103/PhysRevX.9.011036.
- [15] M. Boyarsky, T. Sleasman, M. F. Imani, J. N. Gollub, and D. R. Smith, "Electronically steered metasurface antenna," Sci. Rep., vol. 11, no. 1, p. 4693, Feb. 2021, doi: 10.1038/s41598-021-83377-9.
- [16] T. Sleasman, M. F. Imani, J. N. Gollub, and D. R. Smith, "Dynamic meta-material aperture for microwave imaging," Appl. Phys. Lett., vol. 107, no. 20, p. 204,104, Nov. 2015, doi: 10.1063/1.4935941.
- [17] B. B. Tierney and A. Grbic, "Designing anisotropic, inhomogeneous metamaterial devices through optimization," *IEEE Trans. Antennas Propag.*, vol. 67, no. 2, pp. 998–1009, Feb. 2019, doi: 10.1109/TAP.2018.2883668.
- [18] L. Szymanski, G. Gok, and A. Grbic, "Inverse design of multi-input multi-output 2d metastructured devices," *IEEE Trans. Antennas Propag.*, early access, Dec. 28, 2021, doi: 10.1109/TAP.2021.3137301
- [19] J. R. Sanford, "Design of a miniature reactive beam forming network," in Proc. 2019 IEEE Antennas Propag. Soc. Int. Symp. (APSURSI), pp. 1357–1358, doi: 10.1109/APUSNCURSINRSM.2019.8888916.
- [20] R. Pestourie, C. Pérez-Arancibia, Z. Lin, W. Shin, F. Capasso, and S. G. Johnson, "Inverse design of large-area metasurfaces," *Opt. Exp.*, vol. 26, no. 26, pp. 33,732–33,747, Dec. 2018, doi: 10.1364/OE.26.033732.
- [21] M. Chen, J. Jiang, and J. A. Fan, "Design space reparameterization enforces hard geometric constraints in inverse-designed nanophotonic devices," ACS Photon., vol. 7, no. 11, pp. 3141–3151, 2020, doi: 10.1021/acsphotonics.0c01202.
  [22] S. D. Campbell, D. Sell, R. P. Jenkins, E. B. Whiting, J. A. Fan, and D. H. Werner, "Review of numerical optimization techniques for meta-device design," Opt. Mater. Exp., vol. 9, no. 4, pp. 1842–1863, Apr. 2019, doi: 10.1364/OME.9.001842.
- [23] A. Y. Piggott, J. Lu, K. G. Lagoudakis, J. Petykiewicz, T. M. Babinec, and J. Vuc'kovic', "Inverse design and demonstration of a compact and broadband on-chip wavelength demultiplexer," *Nature Photon.*, vol. 9, no. 6, pp. 374–377, Jun. 2015, doi: 10.1038/nphoton.2015.69.
- [24] C. M. Lalau-Keraly, S. Bhargava, O. D. Miller, and E. Yablonovitch, "Adjoint shape optimization applied to electromagnetic design," *Opt. Exp.*, vol. 21, no. 18, pp. 21,693–21,701, Sep. 2013, doi: 10.1364/OE.21.021693.
- [25] W. Rotman and R. Turner, "Wide-angle microwave lens for line source applications," *IEEE Trans. Antennas Propag*, vol. 11, no. 6, pp. 623–632, Nov. 1963, doi: 10.1109/TAP.1963.1138114.
- [26] C. Pfeiffer and A. Grbic, "A printed, broadband Luneburg lens antenna," IEEE Trans. Antennas Propag., vol. 58, no. 9, pp. 3055–3059, Sep. 2010, doi: 10.1109/TAP.2010.2052582.
- [27] J. Butler, "Beam-forming matrix simplifies design of electronically scanned antennas," *Electron. Des.*, vol. 9, pp. 170–173, Apr. 1961.
- [28] F. Mesa, G. Valerio, R. Rodriguez-Berral, and O. Quevedo-Teruel, "Simulation-assisted efficient computation of the dispersion diagram of periodic structures: A comprehensive overview with applications to filters, leaky-wave antennas and metasurfaces," *IEEE Antennas Propag. Mag.*, vol. 63, no. 5, pp. 33–45, Oct. 2020, doi: 10.1109/MAP.2020.3003210.
- [29] S. Stein, "On cross coupling in multiple-beam antennas," *IRE Trans. Antennas Propag.*, vol. 10, no. 5, pp. 548–557, 1962, doi: 10.1109/TAP.1962.1137917.
   [30] J. D. Kraus, *Antennas*, 2nd ed. New York, NY, USA: McGraw-Hill, 1988.
- [31] C.-T. Tai and C. Pereira, "An approximate formula for calculating the directivity of an antenna," *IEEE Trans. Antennas Propag.*, vol. 24, no. 2, pp. 235–236, Mar. 1976, doi: 10.1109/TAP.1976.1141313.
- [32] C. A. Balanis, Antenna Theory: Analsysis and Design, 3rd ed. Hoboken, NJ, USA: Wiley, 2005.
- [33] L. Schulwitz and A. Mortazawi, "A new low loss Rotman lens design using a graded dielectric substrate," *IEEE Trans. Microw. Theory Techn.*, vol. 56, no. 12, pp. 2734–2741, Dec. 2008, doi: 10.1109/TMTT.2008.2006802.